crystals

MDPI

Article

Nanocrystallization of $Cu_{46}Zr_{33.5}Hf_{13.5}Al_7$ Metallic Glass

Jaskaran S. Saini [1,2,3,†], Tamara D. Koledin [1,2,†], Tittaya Thaiyanurak [1,2], Lei Chen [1,2], Melissa K. Santala [1,2] and Donghua Xu [1,2,*]

[1] Materials Science Program, Oregon State University, Corvallis, OR 97331, USA; melissa.santala@oregonstate.edu (M.K.S.)
[2] School of Mechanical, Industrial and Manufacturing Engineering, Oregon State University, Corvallis, OR 97331, USA
[3] Department of Nanoengineering, University of California, San Diego, CA 92037, USA
* Correspondence: donghua.xu@oregonstate.edu
† These authors contributed equally to this work.

Abstract: The recently discovered $Cu_{46}Zr_{33.5}Hf_{13.5}Al_7$ (at.%) bulk metallic glass (BMG) presents the highest glass-forming ability (GFA) among all known copper-based alloys, with a record-breaking critical casting thickness (or diameter) of 28.5 mm. At present, much remains to be explored about this new BMG that holds exceptional promise for engineering applications. Here, we report our study on the crystallization behavior of this new BMG, using isochronal and isothermal differential scanning calorimetry (DSC), X-ray diffraction (XRD), and transmission electron microscopy (TEM). With the calorimetric data, we determine the apparent activation energy of crystallization, the Avrami exponent, and the lower branch of the isothermal time–temperature–transformation (TTT) diagram. With XRD and TEM, we identify primary and secondary crystal phases utilizing samples crystallized to different degrees within the calorimeter. We also estimate the number density, nucleation rate, and growth rate of the primary crystals through TEM image analysis. Our results reveal that the crystallization in this BMG has a high activation energy of ≈360 kJ/mole and that the primary crystallization of this BMG produces a high number density (≈10^{21} m^{-3} at 475 °C) of slowly growing (growth rate < 0.5 nm/s at 475 °C) $Cu_{10}(Zr,Hf)_7$ nanocrystals dispersed in the glassy matrix, while the second crystallization event further produces a new phase, $Cu(Zr,Hf)_2$. The results help us to understand the GFA and thermal stability of this new BMG and provide important guidance for its future engineering applications, including its usage as a precursor to glass–crystal composite or bulk nanocrystalline structures.

Keywords: metallic glass; crystallization; nucleation and growth; Cu alloys; nano-crystal; amorphous alloys; ImageJ; supercooled liquid; calorimetry

Citation: Saini, J.S.; Koledin, T.D.; Thaiyanurak, T.; Chen, L.; Santala, M.K.; Xu, D. Nanocrystallization of $Cu_{46}Zr_{33.5}Hf_{13.5}Al_7$ Metallic Glass. *Crystals* **2023**, *13*, 1322. https://doi.org/10.3390/cryst13091322

Academic Editor: Vesselin Tonchev

Received: 25 July 2023
Revised: 17 August 2023
Accepted: 18 August 2023
Published: 29 August 2023

1. Introduction

Bulk metallic glasses (BMGs) are a new generation of metallic materials that are dramatically different from conventional engineering metals or alloys [1–5]. They possess an overall disordered structure, without any crystal grains or crystal-related defects (e.g., grain boundaries, dislocations) which widely exist in conventional metals or alloys. Because of this, BMGs exhibit a host of properties far exceeding their crystalline counterparts, such as strength, hardness, wear and corrosion resistance, elastic strain limit, resilience, and magnetic softness (for ferromagnetic BMGs) [1–5]. In addition, they bring out new manufacturing opportunities for the metal industry, for example, thermoplastic processing far below the melting temperature, near-net-shape casting, and microstructure control by partial or full crystallization of the amorphous matrix [6,7].

Nevertheless, a number of challenges remain to be solved before the advantages of BMGs can be widely utilized in industry. Among these is their still limited glass-forming ability (GFA). When a BMG is manufactured (usually by melt casting), its smallest

dimension, which dominates the heat transfer, must be kept below a threshold value in order to obtain fast enough cooling and freeze the melt directly into a disordered (glassy) structure. This threshold is termed the critical casting thickness (or diameter for a cylindrical rod), L_c. The L_c is a manifestation of the GFA and, correspondingly, the manufacturability of a BMG. Unfortunately, most BMGs discovered to date possess a critical casting thickness below 15 mm [8–17], which significantly limits their possible engineering applications. This is a common problem across many different types of BMGs, including copper (Cu)-based BMGs, which are of broad interest due to the attractive characteristics of copper (e.g., low cost, abundant supply, high ductility, high electrical and thermal conductivity).

Recently, a new series of Cu-based BMGs, $Cu_{46}Zr_{47-x}Hf_xAl_7$ ($8 \leq x \leq 20$ at.%), have been discovered at Oregon State University that possess exceptional GFA, with the critical casting thickness exceeding 15 mm [14]. In particular, $Cu_{46}Zr_{33.5}Hf_{13.5}Al_7$ possesses a critical casting thickness of at least 28.5 mm, marking a new record for any Cu-based BMG alloy. Furthermore, unlike the few earlier reported BMGs with similar (or better) GFA, e.g., Zr-Ti-Cu-Ni-Be, Pd-Cu-Ni-P, Mg-Cu-Ag-Gd, and La-Al-Cu-Ag-Ni-Co [8], these new Cu-Zr-Hf-Al BMGs are free of toxic elements (e.g., Be), precious metals (e.g., Pd, Ag), and rare earths (e.g., Gd, La), which makes them even more attractive for engineering applications. At present, much remains to be explored about these new Cu-Zr-Hf-Al BMGs, for example, the origin of GFA, thermal stability, atomic structure (chemical and topological short-range ordering), mechanical properties (elastic and plastic deformation mechanisms), and electrical properties.

Here, we focus on the crystallization behavior of the $Cu_{46}Zr_{33.5}Hf_{13.5}Al_7$ BMG, which has the highest GFA among all Cu-based BMGs. Studying crystallization behavior may help us to understand the GFA and thermal stability and guide future engineering applications of this exceptional BMG, including its usage as a precursor to glass–crystal composite and bulk nano-crystalline structures. We perform isochronal (constant heating rate) and isothermal differential scanning calorimetry (DSC) experiments on as-cast samples to determine the apparent activation energy of crystallization, the Avrami exponent, and the lower branch of the isothermal time–temperature–transformation (TTT) diagram. We also perform X-ray diffraction (XRD) and transmission electron microscopy (TEM) on samples crystallized to different degrees within the calorimeter to identify the primary and secondary crystal phases and estimate the number density and nucleation and growth rates of the primary crystals. We discuss our results in connection with the GFA, thermal stability, and potential applications of the $Cu_{46}Zr_{33.5}Hf_{13.5}Al_7$ BMG.

2. Experimental Methods

An alloy ingot of the $Cu_{46}Zr_{33.5}Hf_{13.5}Al_7$ BMG was produced by arc melting (after ultrasonic cleaning) Cu (oxygen-free shots), Zr (crystal bar), Hf (crystal bar), and Al pieces with purities of 99.99%, 99.9+%, 99.2+%, and 99.99%, respectively, on a water-cooled copper stage that was tiltable from outside the arc melting chamber. Prior to melting, the chamber was pumped to a high vacuum with a residual pressure of 3×10^{-4} mbar and then filled with ultrahigh-purity argon. The atmosphere was then further purified by first melting a Zr getter (placed at a separate position) before melting the Cu, Zr, Hf, and Al pieces. The $Cu_{46}Zr_{33.5}Hf_{13.5}Al_7$ alloy ingot was flipped and remelted eight times in the arc melter in order to obtain complete chemical homogeneity. The alloy ingot was then melted once again and tilt cast into a copper mold placed below the melting stage that has a 10 mm diameter cylindrical cavity. Small specimens were then cut from the cast rod using a high-speed diamond saw and used for DSC, XRD, and TEM experiments.

A Mettler Toledo DSC 3 with platinum pans and flowing ultrahigh-purity nitrogen was used for thermal analysis and for preparing XRD and TEM specimens with controlled degrees of crystallization. A range of heating rates from 2.5 to 40 K/min were employed for isochronal DSC. For isothermal DSC, the specimens were heated at a relatively high heating rate of 60 K/min to a target temperature and held there until the completion of crystallization. A set of holding temperatures ranging from 470 to 500 °C was utilized for

the isothermal DSC. In order to characterize the primary crystallization phase using XRD and TEM, an additional specimen was isothermally held at 475 °C inside the calorimeter just past the first exothermic peak and then quickly (≈150 K/min) cooled back to room temperature.

This partially crystallized specimen, an as-cast specimen, and a fully crystallized (also at 475 °C) specimen were studied using XRD and TEM. For XRD, a Rigaku Smartlab X-ray diffractometer was used with a Cu-Kα source in a reflection (Bragg–Brentano) mode with θ-θ scan.

Specimens were prepared for TEM by cutting the materials into 3 mm diameter disks, thinning them to ≈40 µm, and polishing one side to a mirror finish with diamond paste. The second side was dimpled and polished with diamond paste, reducing the thickness to ≈15 µm. Specimens were then ion milled to perforation with argon at 5 keV, followed by 10 min at 2 keV. These accelerating voltages were carefully chosen to prevent ion-milling-induced phase transformations [18]. An FEI Titan TEM/STEM operated at 200 keV was used to take bright-field images of the microstructure and perform selected area electron diffraction (SAED).

3. Results and Discussion

3.1. Isochronal DSC

Figure 1 shows the exothermic DSC signals caused by crystallization during continuous isochronal heating at rates of 2.5, 5, 10, 15, 20, 25, 30, 35, and 40 K/min. As the heating rate increased, the DSC peak shifted to higher temperatures, which was as expected (due to less time spent at each temperature). At the two lowest heating rates, i.e., 2.5 and 5 K/min, the DSC peak displayed two minor splittings that were close to each other, indicating that the crystallization proceeded with two steps: primary and secondary crystallization events. At the other (higher) heating rates, no peak splittings were apparent, most likely due to the overlap between the two steps at the higher crystallization temperatures. Indeed, the increasing overlap between the two crystallization events at a higher heating rate is recognizable if one compares the DSC signals for the 2.5 and 5 K/min heating rates.

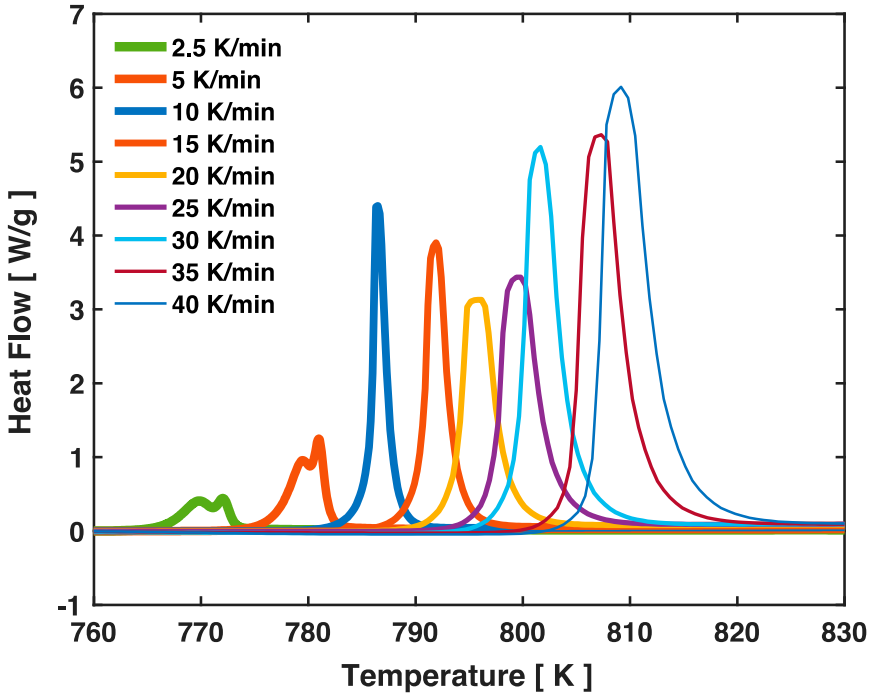

Figure 1. Crystallization signals (exothermic) recorded in isochronal DSC scans of as-cast specimens at nine different heating rates.

Kissinger's method is often used to analyze the correspondence between the DSC peak shift and the heating rate to extract an overall activation energy of a thermally activated process (e.g., chemical reaction or phase transformation) [19–21]. This method is based on the first-order chemical reaction model and, more specifically, the following equation:

$$\frac{dx}{dt} = A\ \exp\left(-\frac{E_a}{RT}\right)(1-x) \tag{1}$$

in which x is the dimensionless reacted (or transformed) fraction. This equation assumes that the reaction rate, dx/dt, is proportional to the remaining unreacted fraction $1-x$ and that the proportionality coefficient or reaction rate constant is solely determined by the temperature, T, according to the Arrhenius formulation, which contains activation energy, E_a, universal gas constant, R, and pre-exponential factor, A.

Based on Equation (1) and the fact that the heat flow measured by DSC is essentially dx/dt (scaled by the total enthalpy of crystallization, i.e., the total area enclosed by the DSC peak), a relationship between the peak position (temperature), T_p, on the DSC signal, where the dx/dt is at its maximum, and the heating rate β employed in an isochronal scan can be theoretically derived by taking the derivative of Equation (1) on both sides (note that T varies linearly with t as $dT/dt = \beta$) and setting that to zero. The result is the well-known Kissinger's equation:

$$\ln\left(\frac{\beta}{T_p^2}\right) = -\frac{E_a}{R}\frac{1}{T_p} + \ln A - \ln\frac{E_a}{R} \tag{2}$$

which suggests a linear correlation between $\ln\left(\frac{\beta}{T_p^2}\right)$ and $\frac{1}{T_p}$ with a slope equal to $-\frac{E_a}{R}$. Once the slope is known, the activation energy E_a can be conveniently determined.

Figure 2 presents the so-called Kissinger plot of $\ln\left(\frac{\beta}{T_p^2}\right)$ vs. $\frac{1}{T_p}$, showing both experimental data and the fitted linear correlation. The Kissinger model captured the experimental data quite well, with a fitting goodness (R^2) of 0.986. Using the slope from the linear fitting, the activation energy E_a for the crystallization was determined to be 360 kJ/mole.

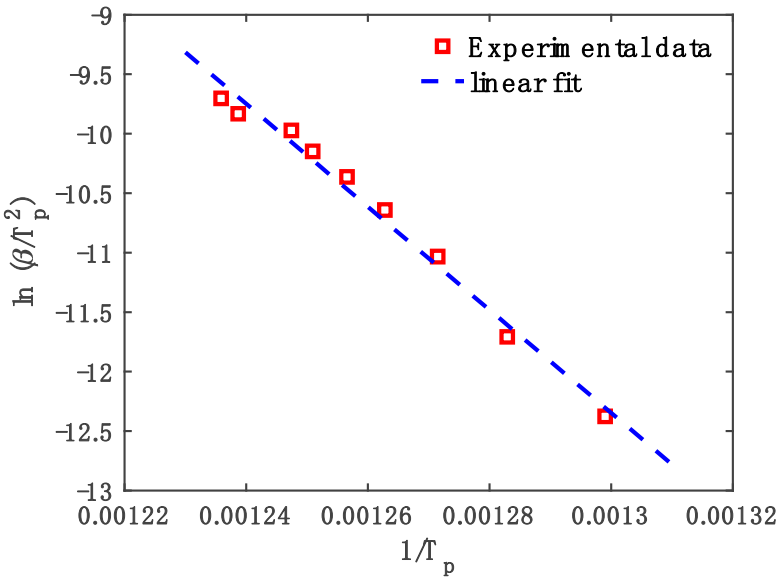

Figure 2. Kissinger plot based on the crystallization peaks in the isochronal DSC scans of as-cast specimens.

In Figure 2, the data points representing the two lowest heating rates (2.5 and 5 K/min) are based on the first peak-splitting of the DSC signal, as shown in Figure 1. If the second peak-splitting was used for these two heating rates (while data remained the same for the

other heating rates), the Kissinger fitting was still reasonably good, albeit with a slightly lower R^2 of 0.977, and the activation energy E_a was determined to be 380 kJ/mole, even higher than the 360 kJ/mole reported above.

The values of E_a obtained here are larger than those reported for most other Cu-based metallic glasses in the literature, for example, 208 kJ/mole for $Cu_{73}Sn_6Ni_6P_{15}$ [22], 331 kJ/mole for $Cu_{50}Zr_{40}Ti_{10}$ [23], and 354 kJ/mole for $Cu_{43}Zr_{43}Al_7Ag_7$ [24]. A high activation energy for crystallization is generally in line with a high GFA because glass formation requires the avoidance of crystallization (although glass is made most commonly through a cooling instead of a heating process). Hence, the results here contribute to our understanding of the origin of the superior GFA of the $Cu_{46}Zr_{33.5}Hf_{13.5}Al_7$ BMG. From another perspective, a high activation energy for crystallization widens the temperature window for controlling the crystallization process so as to produce preferred microstructural characteristics (e.g., crystallite number density, grain size, remaining glass fraction) in the devitrified glass.

Note that Equation (1), i.e., the first-order chemical reaction model with a reaction rate constant solely decided by the temperature, as assumed in Kissinger's method, is not strictly valid for phase transformations such as crystallization. A simple piece of evidence is that at a fixed temperature (and varying time), Equation (1) predicts an exponential decay of the DSC signal, which is not the case, as is discussed in the next section of this paper and in the vast literature on isothermal DSC studies. Indeed, the Kolmogorov–Johnson–Mehl–Avrami (KJMA) model combined with appropriate descriptions for crystal nucleation and growth rates, which, in whole, is equivalent to Equation (1) but with a time-dependent (power law) rate constant, is more applicable to phase transformations. Nonetheless, the Kissinger analysis does provide an overall activation energy that largely represents how difficult it is for crystallization to occur and that can be conveniently compared across different materials.

3.2. Isothermal DSC

Figure 3 shows the isothermal DSC scans (heat flow vs. time) of the $Cu_{46}Zr_{33.5}Hf_{13.5}Al_7$ BMG obtained at seven different temperatures ranging from 470 to 500 °C. These temperatures were all above the apparent glass transition temperature, 454 °C, observed during the preheating (60 K/min) prior to the isothermal holding. All the isothermal scans displayed two crystallization events (peaks), and the two events became more and more overlapped with increasing temperature. This is consistent with observations from the isochronal DSC scans (especially those at 2.5 and 5 K/min heating rates).

The basic form of the KJMA model for phase transformations is as follows:

$$dx = dx_{ext}(1 - x) \tag{3}$$

where x is the actual transformed fraction and x_{ext} is the extended transformed fraction. x_{ext} is a fictive quantity theoretically determined by integrating nucleation and growth rates over time without considering any spatial overlap of nuclei/grains or the continuous decrease of the remaining parental phase that limits later transformation. Generally, the extended fraction is expressed as $x_{ext} = \lambda t^m$, where t is the time, m is the so-called Avrami exponent, and λ is a rate constant that comprises contributions from both nucleation and growth rates. Combining Equation (3) and the power law of x_{ext}, one can find $x = 1 - \exp(-\lambda t^m)$ and its differential form:

$$\frac{dx}{dt} = \lambda m t^{m-1} \exp(-\lambda t^m) \tag{4}$$

which is a single-event KJMA model for an isothermal DSC signal (after baseline removal and normalization). Equation (4) assumes that nucleation and growth of the new phase start

from time zero. When there is an incubation period t_i, as is often encountered, Equation (4) can be modified as follows:

$$\frac{dx}{dt} = \lambda m(t - t_i)^{m-1} \exp\left[-\lambda(t - t_i)^m\right] \tag{5}$$

Since there are two crystallization events here, the two-event version of the KJMA model:

$$\begin{array}{c} \frac{dx}{dt} = f_1\lambda_1 m_1(t - t_{i1})^{m_1-1} \exp\left[-\lambda_1(t - t_{i1})^{m_1}\right] \\ +(1 - f_1)\,\lambda_2 m_2(t - t_{i2})^{m_2-1} \exp\left[-\lambda_2(t - t_{i2})^{m_2}\right] \end{array} \tag{6}$$

was used to fit the isothermal DSC data in this study, where f_1 is the total fraction of transformation contributed by the first event. Care needs to be taken to properly implement this fitting. For example, to avoid imaginary numbers and associated numerical problems, the $t - t_{i1}$ and $t - t_{i2}$ should be compared with zero and replaced by zero, if negative, by the fitting program.

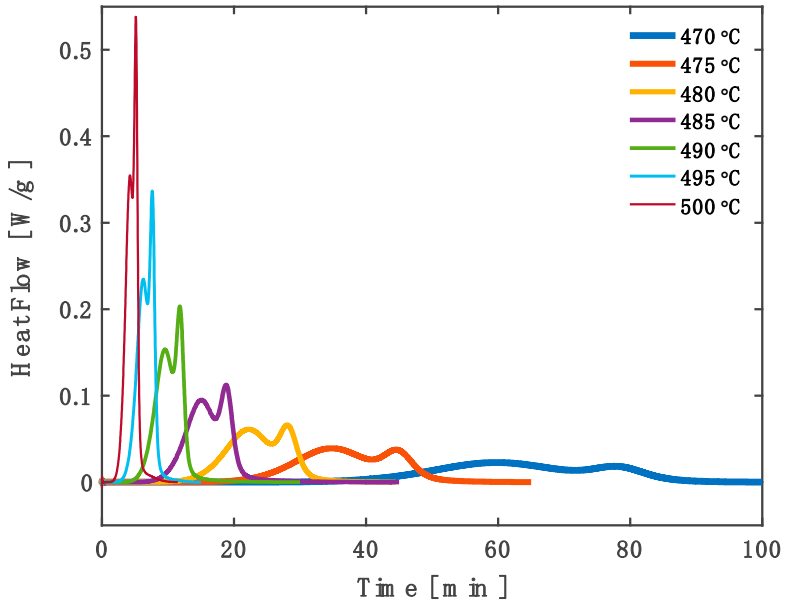

Figure 3. Crystallization signals (exothermic) recorded in isothermal DSC scans of as-cast specimens at seven different temperatures.

The two-event KJMA model fit the data very closely, with $R^2 > 0.99$ achieved for all seven temperatures. Examples of the fitted curves (the normalization factor, i.e., the total enthalpy of crystallization, reapplied for plotting) vs. experimental data are presented in Figure 4 with T = 475, 485, and 495 °C. The fitting results for the seven different temperatures are tabulated in Table 1. The fitted Avrami exponents (m_1, m_2) and incubation times (t_{i1}, t_{i2}) of the primary and secondary crystallization events are plotted in Figure 5. As seen in Table 1 and Figure 5, the incubation time decreased with increasing temperature for both events. At 470 °C (16 °C above the glass transition temperature), the incubation time was rather long: 23.4 min for the primary event and 68.2 min for the secondary event. At 500 °C, it became significantly shorter: 0.5 min and 4.6 min for the primary and secondary events, respectively.

The Avrami exponent increased from 4.4 at 470 °C to 6.4 at 500 °C for the primary crystallization, while it stayed fairly stable around 2.6 to 2.8 for the secondary crystallization. In the standard theory, the Avrami exponent is expected to range from 0.5 (instantaneous/heterogeneous nucleation and 1-D diffusion-controlled growth) to 4 (homogeneous nucleation and 3-D interface-controlled growth). More specifically, if the nucleation is homogeneous, the Avrami exponent is expected to take values of 2, 3, and 4 for 1-D, 2-D,

and 3-D interface-controlled growth and 1.5, 2, and 2.5 for 1-D, 2-D, and 3-D diffusion-controlled growth, respectively. If the nucleation is instantaneous/heterogeneous, these expected values all decrease by 1. Apparently, the Avrami exponents obtained here did not fit into any of the standard cases.

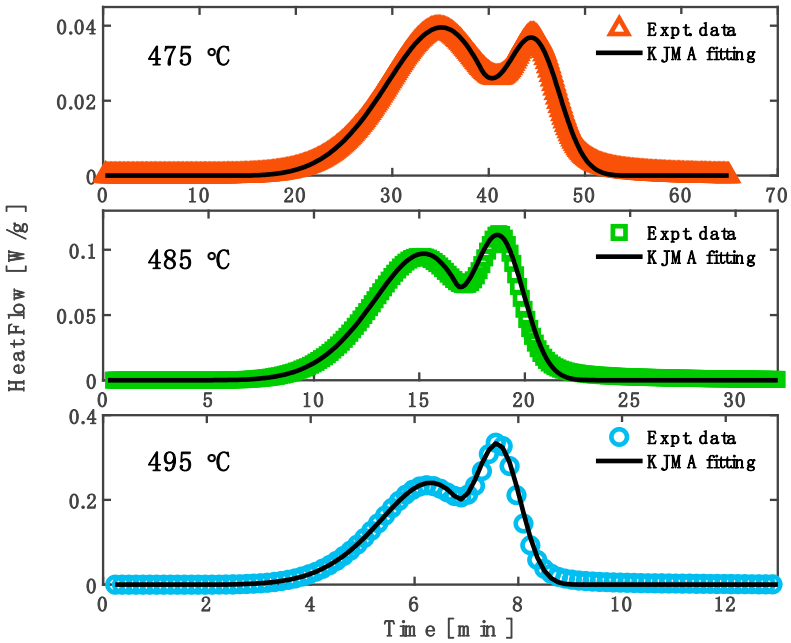

Figure 4. Examples of two-event KJMA model fitting of the isothermal DSC data.

Table 1. Two-event KJMA fitting results at seven temperatures.

T	f_1	λ_1	m_1	t_{i1} (min)	λ_2	m_2	t_{i2} (min)
470 °C	0.77	1.1×10^{-7}	4.37	23.43	8.7×10^{-4}	2.84	68.17
475 °C	0.73	1.8×10^{-7}	4.86	11.74	5.1×10^{-3}	2.78	39.26
480 °C	0.71	1.6×10^{-7}	5.50	5.80	0.020	2.77	24.82
485 °C	0.69	5.5×10^{-7}	5.77	3.45	0.086	2.55	16.80
490 °C	0.68	4.4×10^{-6}	5.97	1.97	0.24	2.75	10.46
495 °C	0.68	2.1×10^{-5}	6.35	0.99	0.92	2.76	6.80
500 °C	0.68	1.8×10^{-4}	6.39	0.53	2.70	2.63	4.60

The rising trend and the values of the Avrami exponent obtained here for the primary crystallization can be understood as the result of an increasing degree of non-steadiness of homogeneous nucleation that was implied by the diminishing incubation time. At 470 °C, the incubation time was very long and the supercooled liquid matrix adjusted its topological and chemical short-range ordering (which is well known to exist in metallic glasses and their supercooled liquids [25–30]) and prepared for homogeneous nucleation in an approximately steady manner. The nearly steady-state homogeneous nucleation combined with 3-D interface-controlled growth (the 3-D dimensionality of the primary crystals can be observed from the TEM images in Section 3.4) resulted in an Avrami exponent of 4.4, only slightly above the standard value of 4. At higher holding temperatures, the incubation time became notably shorter and the local structural and chemical adjustment of the supercooled liquid matrix and the homogeneous nucleation of the primary crystal phase became increasingly non-steady, i.e., more dependent on time. This additional dependence on time was then manifested by the increase in the Avrami exponent.

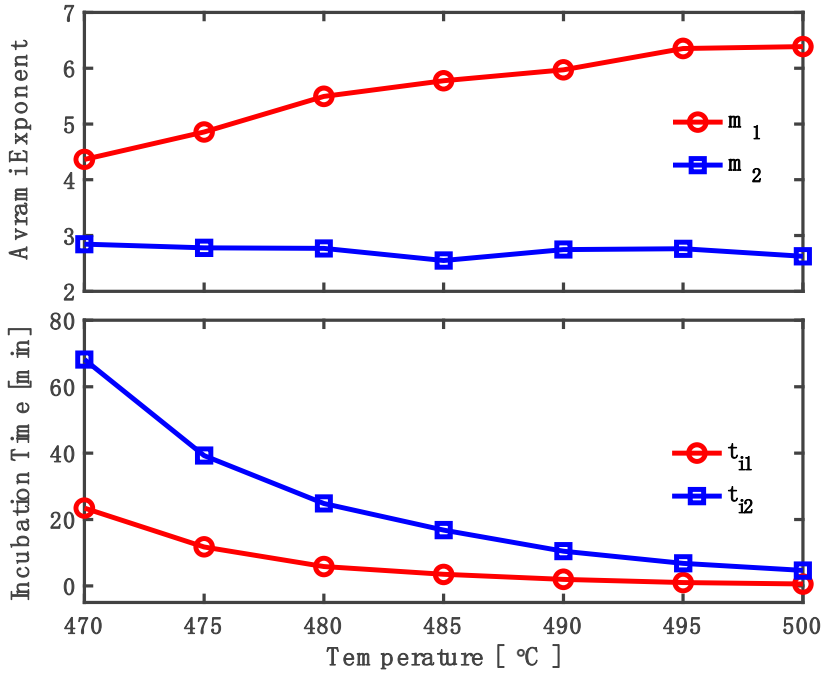

Figure 5. Fitted Avrami exponents (m) and incubation times (t_i) of the primary (subscript 1, i.e., m_1, t_{i1}) and secondary (subscript 2, i.e., m_2, t_{i2}) crystallization events, plotted as a function of temperature.

The stability and the values of the Avrami exponent obtained here for the secondary crystallization can be understood as resulting from heterogeneous nucleation and a sub-3-D growth mode. It is conceivable that the primary crystals formed in the first crystallization event provide heterogeneous nucleation sites for the secondary crystallization and, in the meantime, reduce (to below 3-D) the effective dimensionality of crystal growth in the second event as these secondary crystals grew from the surfaces of the primary crystals towards the remaining supercooled liquid matrix. This resulted in the fairly stable Avrami exponent of around 2.6–2.8 for the secondary crystallization, which was slightly below the standard value of 3 for heterogeneous nucleation combined with a 3-D growth mode.

From the isothermal DSC data presented in Figure 3, one can calculate the cumulative transformation curves (using numerical integration), which are displayed in Figure 6. Due to the existence of two crystallization events, the cumulative transformation curves all showed a kink, although this was less noticeable at higher holding temperatures due to increased overlap between the primary and secondary crystallization events (see Figure 3).

The cumulative transformation curves can be used to extract the time it took to reach certain transformed fractions at varied temperatures and construct isothermal TTT diagrams. Figure 7 exhibits two TTT diagrams obtained here for the $Cu_{46}Zr_{33.5}Hf_{13.5}Al_7$ BMG: one representing a transformed fraction of 1% and the other representing a transformed fraction of 50%, together with the incubation time (for the first crystallization event) as a reference. A complete TTT diagram would exhibit a "C"-shape, with long transformation times in both high-temperature (upper branch) and low-temperature (lower branch, determined here) regimes. The upper branches of the TTT diagrams were not determined here since isothermal holding in that temperature regime would require a very high heating rate (typically available on a flash DSC) or the full melting of the sample followed by rapid cooling to reach those target temperatures, which was beyond the capability of our instrument. Nonetheless, the lower branches of the TTT diagrams obtained here carry particular significance for informing the thermoplastic processing and controlled devitrification of the BMG and predicting the thermal stability of the BMG in applications at moderately elevated temperatures.

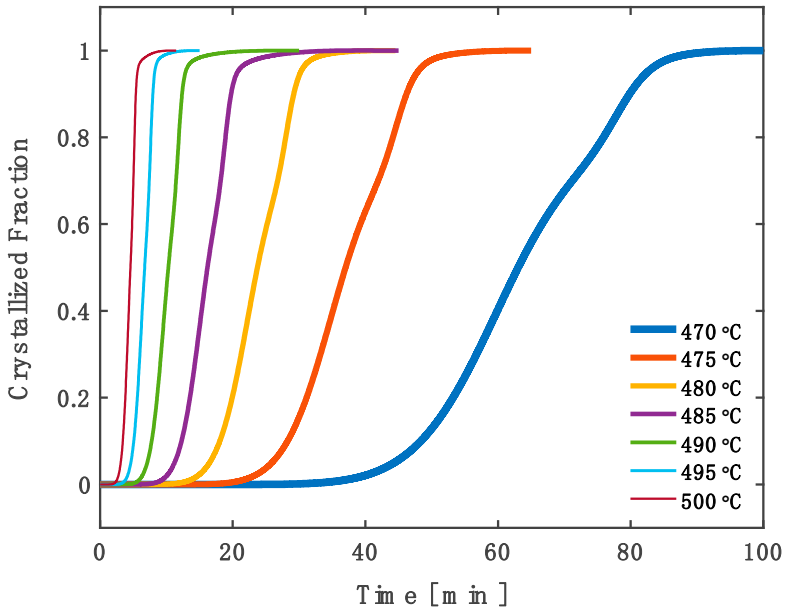

Figure 6. Cumulative transformation curves derived from the isothermal DSC scans at seven different temperatures.

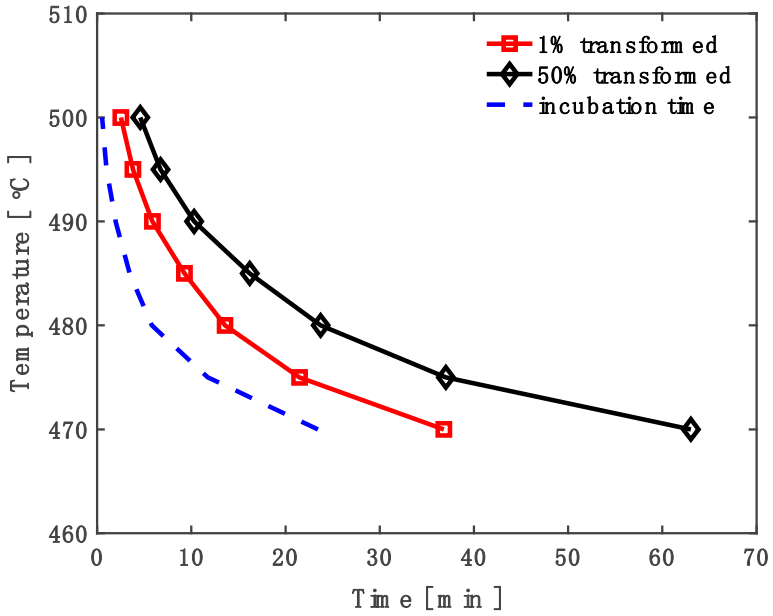

Figure 7. Time–temperature–transformation (TTT) diagrams derived from the cumulative transformation curves.

3.3. X-ray Diffraction (XRD)

Figure 8a shows the XRD pattern of the as-cast specimen of the $Cu_{46}Zr_{33.5}Hf_{13.5}Al_7$ BMG. It consisted of only diffuse/broad maxima (two in the scanned 25 to 80° range of 2θ), without any sharp Bragg peaks. This demonstrates the fully amorphous (glassy) structure of the as-cast specimen.

In Figure 8b, the thick gray line is the XRD pattern obtained from the specimen isothermally annealed inside the calorimeter at 475 °C for 34 min. This annealing time corresponded to the DSC peak of the primary crystallization event at this temperature (see Figure 3) and was shorter than the incubation time for the secondary crystallization event (see Table 1). Thus, only the primary crystal phase was expected to exist in this specimen. The open-source software Profex [31] was used to fit the XRD pattern through

Rietveld refinement. As shown in Figure 8b, this XRD pattern was fitted very nicely with an amorphous phase and a single-crystal phase: $Cu_{10}(Zr,Hf)_7$. The binary compounds $Cu_{10}Zr_7$ and $Cu_{10}Hf_7$ share the same structure (space group 64, Cmce, orthorhombic lattice) and similar lattice parameters [32,33] and, hence, both Zr and Hf were considered to be present in the primary crystal phase. The strong amorphous signal which was directly visible in the experimental data and further confirmed by the fitting suggests that the primary crystals co-existed with a substantial amount of remaining glass matrix, i.e., the specimen had a glass–crystal composite structure.

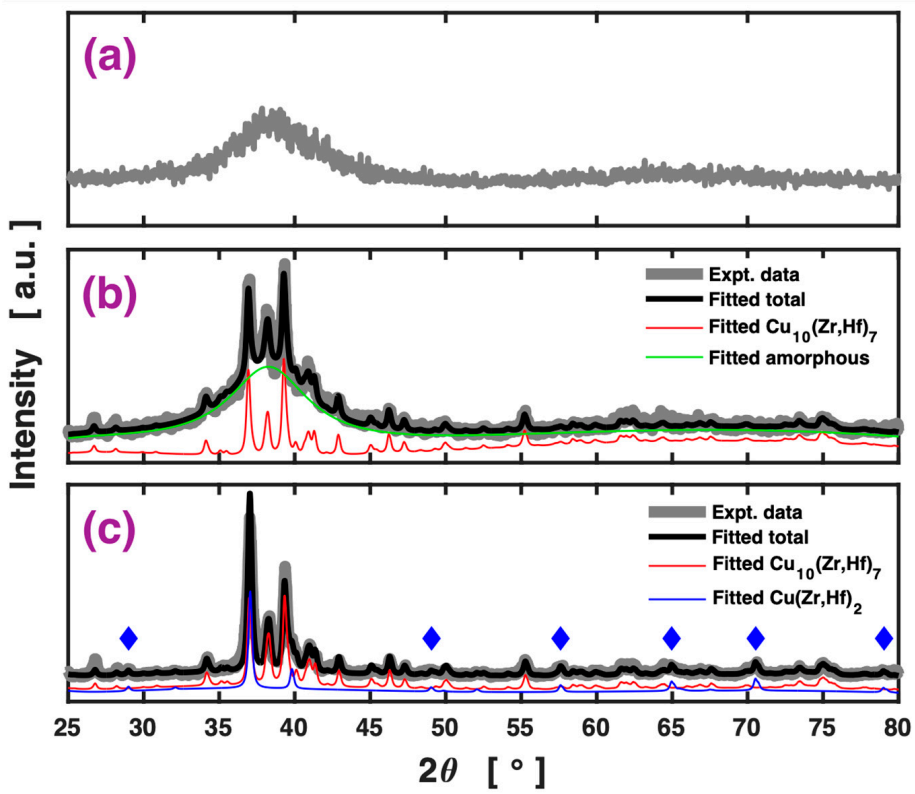

Figure 8. X-ray diffraction patterns (thick gray lines) of the as-cast specimen (**a**), the specimen annealed at 475 °C for 34 min (**b**), and the specimen annealed at 475 °C for 65 min (**c**). For the latter two specimens, fitted total and individual components using Rietveld refinement are also presented. The fitted individual components have been shifted in the y-direction for clarity. The symbols in (**c**) mark the peaks that do not exist in (**b**).

The thick gray line in Figure 8c is the XRD pattern obtained from the specimen isothermally annealed inside the calorimeter at 475 °C for 65 min. According to the isothermal DSC data, this annealing time was longer than it took for both primary and secondary crystallization events to complete at this temperature (see Figure 3). Thus, this specimen was expected to be fully crystallized and comprise both primary and secondary crystal phases. Indeed, the XRD pattern exhibited no appreciable amorphous component, confirming that the specimen was fully crystallized. The Rietveld refinement found a few new peaks (positions marked with blue diamonds) that could not be reproduced using the primary phase $Cu_{10}(Zr,Hf)_7$. These new peaks were found to agree with the $Cu(Zr,Hf)_2$ phase (space group 139, I4/mmm, tetragonal lattice). By considering both the $Cu_{10}(Zr,Hf)_7$ and the $Cu(Zr,Hf)_2$ phases, the whole XRD pattern was found to be well-fitted. The fitting also suggested that the secondary phase $Cu(Zr,Hf)_2$ contributed to the main diffraction peaks near 37° and 39.3° in addition to the marked new peaks.

3.4. Transmission Electron Microscopy (TEM)

Figure 9 presents the bright-field images and overall SAED patterns of the same three specimens as in Section 3.3: one as-cast (a), one annealed at 475 °C for 34 min (b), and one annealed at 475 °C for 65 min (c). The TEM image of the as-cast specimen is smooth and featureless (note that the contrast at the lower left corner is due to thickness variation), typical of amorphous materials. The diffraction pattern consisting of two diffuse rings further confirms the amorphous structure of the specimen. This is also consistent with the XRD result presented in Figure 8a.

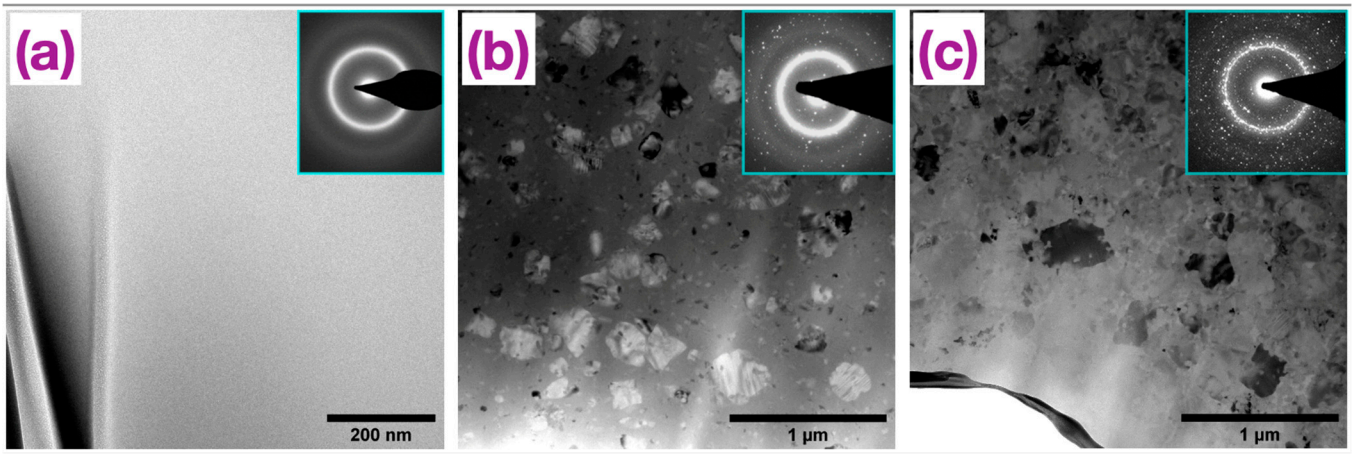

Figure 9. TEM bright-field images and SAED patterns (inset) of the as-cast specimen (**a**), the specimen annealed at 475 °C for 34 min (**b**), and the specimen annealed at 475 °C for 65 min (**c**).

The TEM image of the specimen annealed at 475 °C for 34 min in Figure 9b exhibited nearly equiaxed crystals of various sizes embedded in a featureless matrix. The corresponding overall SAED pattern was composed of both diffuse amorphous rings and discrete spots from crystal grains. Both the image and the diffraction pattern confirm the glass–crystal composite structure of this partially crystallized specimen, consistent with the XRD data in Figure 8b.

To verify the $Cu_{10}(Zr,Hf)_7$ primary crystal phase identified from the XRD data analysis, more targeted SAED patterns were collected of single grains in the partially crystallized specimen by isolating the grains with a selected area aperture. Figure 10b shows an example of a single-crystal-like diffraction pattern taken from the grain marked in Figure 10a. The pattern was found to closely match the [0 1 1] zone axis pattern of $Cu_{10}Zr_7$ in the ICDD (International Centre for Diffraction Data [33]) database (PDF Card #01-082-3014) that is shown in Figure 10c. As mentioned earlier in Section 3.3, binary compounds $Cu_{10}Zr_7$ and $Cu_{10}Hf_7$ possess the same structure and similar lattice parameters and, hence, this reference pattern is representative of $Cu_{10}(Zr,Hf)_7$ with random substitution of Zr and Hf on their sublattice. The close match between the measured and reference electron diffraction patterns here provides additional support for the $Cu_{10}(Zr,Hf)_7$ as the primary crystal phase, affirming the earlier XRD analysis.

The TEM image (Figure 9c) of the specimen annealed at 475 °C for 65 min showed the relatively bigger primary crystals together with the finer microstructure in between them throughout the specimen, the latter attributable to the second crystallization event. The overall diffraction pattern comprised a high density of spots, some of which appeared to have connected into a thin ring that is typical of a polycrystalline structure with random grain orientations. Selective diffraction targeting the finer microstructure between the primary crystals resulted in a complex moiré pattern due to double diffraction events involving two crystalline phases, as shown in Figure 11b (taken from the grain marked in Figure 11a). The pattern resembles a superimposition of the [1 0 0] pattern of $Cu_{10}Zr_7$ and the [0 0 1] pattern of the $CuZr_2$ (PDF Card 04-002-0044, same structure as $CuHf_2$) in the ICDD database, which are displayed in Figure 11c,d, respectively, with additional

spots from the moiré. This affirms the conclusion from the XRD analysis that $Cu(Zr,Hf)_2$ is a new phase produced in the second crystallization event. The double diffraction with superimposed $Cu(Zr,Hf)_2$ and $Cu_{10}(Zr,Hf)_7$ patterns is believed to be caused by the technical difficulty in finding a single $Cu(Zr,Hf)_2$ grain that is not interrupted by primary $Cu_{10}(Zr,Hf)_7$ crystals upon diffraction, because the $Cu(Zr,Hf)_2$ grains are very small.

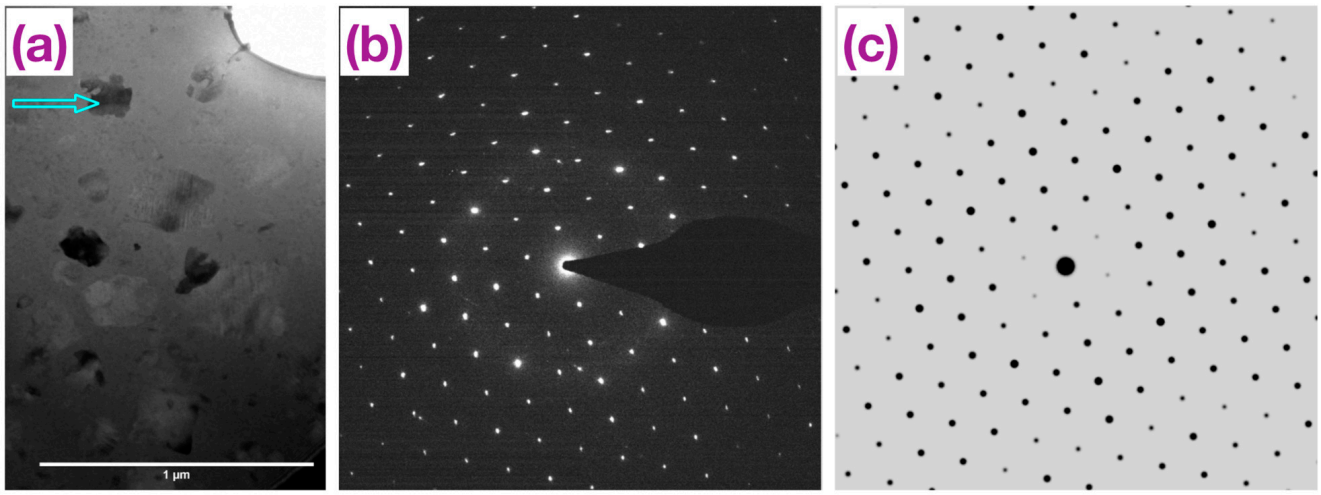

Figure 10. (**a**) TEM bright-field image of the specimen annealed at 475 °C for 34 min; (**b**) single-crystal-like SAED pattern taken from the grain pointed out by the arrow in (**a**); (**c**) simulated electron diffraction pattern of $Cu_{10}Zr_7$ with the zone axis [0 1 1] (ICDD database PDF Card #01-082-3014).

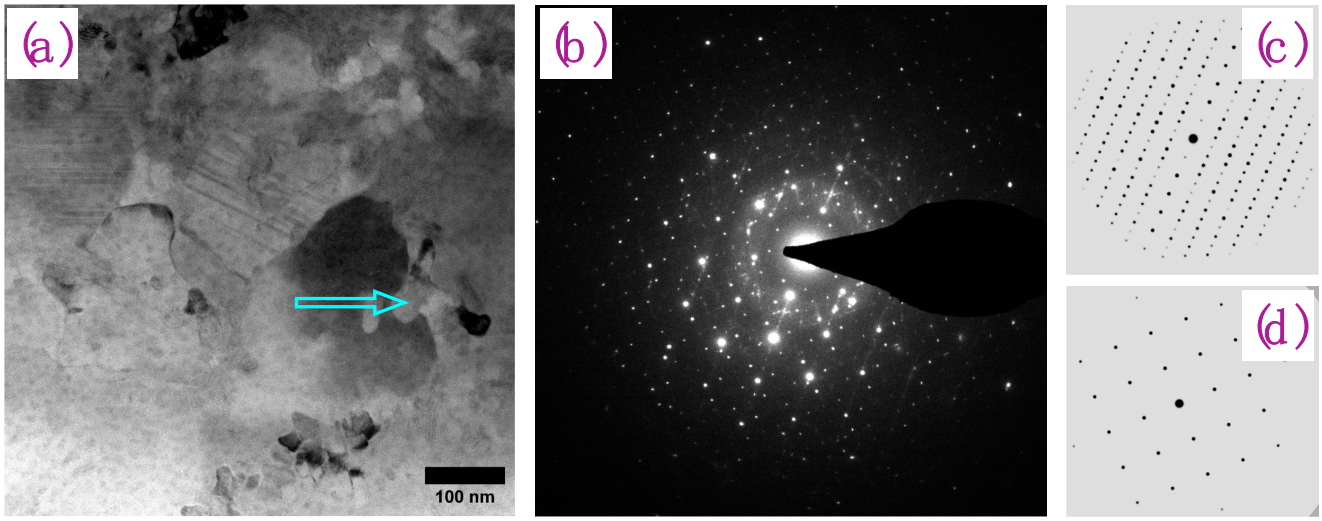

Figure 11. (**a**) TEM bright-field image of the specimen annealed at 475 °C for 65 min; (**b**) SAED pattern taken from the grain pointed out by the arrow in (**a**); (**c**) simulated electron diffraction pattern of $Cu_{10}Zr_7$ with the zone axis [1 0 0] (ICDD database PDF Card #01-082-3014); (**d**) simulated electron diffraction pattern of $CuZr_2$ with the zone axis [0 0 1] (ICDD database PDF Card 04-002-0044).

Finally, we made some broad estimates of number density and nucleation and growth rates of the primary crystals based on the TEM image (Figure 9b) of the specimen annealed at 475 °C for 34 min. The open-source program ImageJ [34] was used to perform particle (here, crystal grains) analysis of the TEM image. The identified grains are shown in Figure 12, the total number of which was 599. The areal fraction of the identified grains with respect to the entire image is 27%. According to the cumulative transformation curves in Figure 6, the transformed fraction corresponding to 34 min at 475 °C is 34%. These two fractions are in quite good agreement, especially if one considers the differences

between the area-based statistics in the 2-D image analysis here and the heat-based (close to but not exactly the same as 3-D volume-based) statistics in the DSC data analysis.

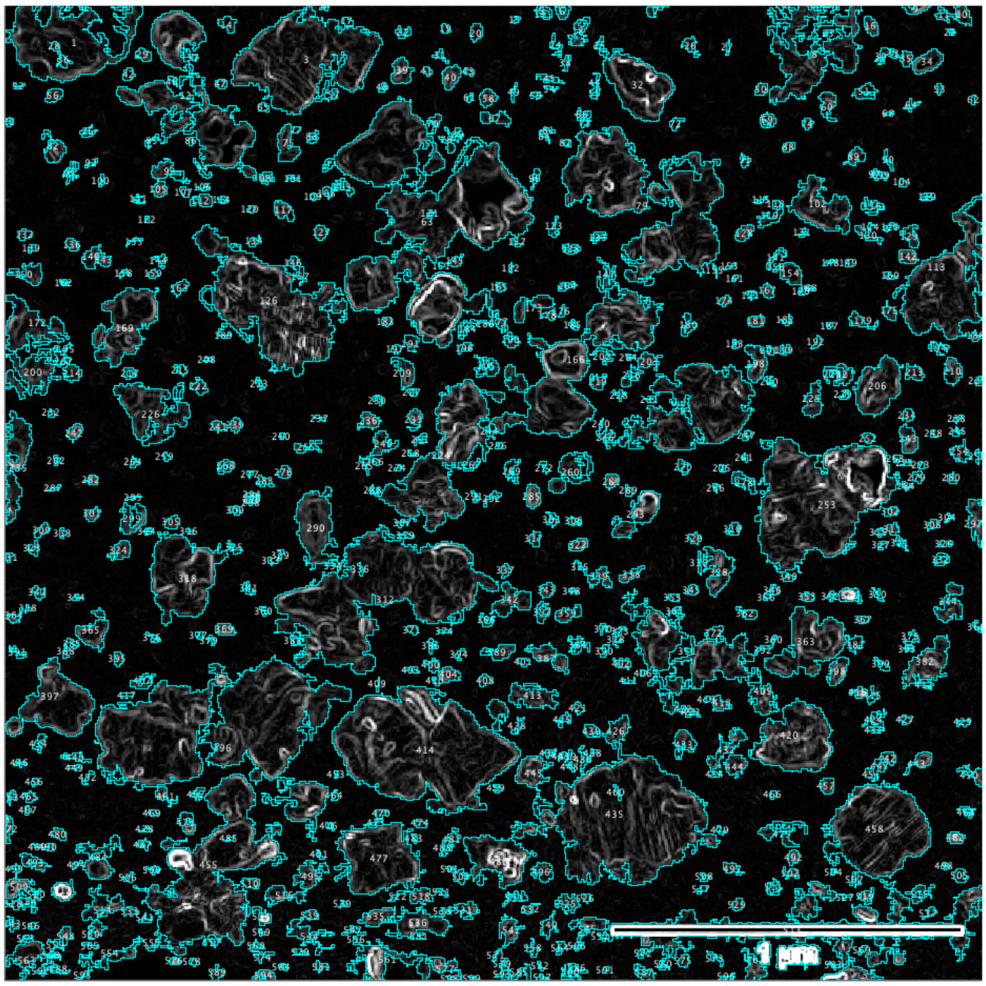

Figure 12. Particle (crystal grain) analysis for the TEM image (Figure 9b) of the specimen annealed at 475 °C for 34 min. The scale bar is 1 μm, the same as in Figure 9b.

The number density of the primary crystals was estimated to be 1.6×10^{21} m^{-3} using the total number of identified grains, the area of the image (2.75 × 2.75 μm), and the approximated thickness of the TEM foil in this region (50 nm). This number density is many orders of magnitude higher than the grain population (≈10^{12} to 10^{15} m^{-3}) in conventional metals/alloys that typically have a tens-of-micron grain size. This comes as a result of the deeply supercooled state of the crystallizing liquid (here, glass heated above its glass transition temperature), which favors the nucleation of new nuclei over the growth of existing ones.

Using the number density and the annealing time (deducting the ≈12 min incubation time revealed by DSC data analysis), the nucleation rate of the primary crystals was estimated to be 1.2×10^{18} m^{-3} s^{-1}. This is on the same order of magnitude as the maximum nucleation rate previously reported [35] for $Pd_{40}Cu_{30}Ni_{10}P_{20}$, another BMG with outstanding glass-forming ability that is based on the precious metal Pd. On the other hand, this nucleation rate is more than ten orders of magnitude higher than the maximum nucleation rate [35] in $Zr_{41.2}Ti_{13.8}Cu_{12.5}Ni_{10}Be_{22.5}$, yet another well-known BMG with an outstanding glass-forming ability which contains a substantial amount of the toxic element Be.

To estimate the growth rate, the biggest primary crystals in the TEM image (Figure 9b) that had a diameter of ≈500 nm were considered to have nucleated and started to grow at

the end of the incubation time (12 min) and, hence, had grown over a time period of 22 min. This yielded an approximate growth rate of 0.38 nm/s, which is extremely low.

It is noted that these estimates of crystal number density and nucleation and growth rates are only for 475 °C and an annealing time of up to 34 min. Nevertheless, they do suggest that the high glass-forming ability of the $Cu_{46}Zr_{33.5}Hf_{13.5}Al_7$ BMG is mainly due to the slow crystal growth, similar to the case of $Pd_{40}Cu_{30}Ni_{10}P_{20}$. The estimated high nucleation rate together with the low crystal growth rate implies a good opportunity to control the crystallization of the BMG towards glass–nanocrystal composite or fully nanocrystalline structures.

4. Conclusions

We have investigated the crystallization behavior of the newly discovered Cu-based $Cu_{46}Zr_{33.5}Hf_{13.5}Al_7$ BMG using DSC, XRD, and TEM. Our main conclusions are as follows:

- Isochronal DSC data revealed a high activation energy of ≈360 kJ/mole for crystallization, consistent with the high glass-forming ability of the alloy.
- Isothermal DSC data at seven different temperatures (470 to 500 °C) were all well fitted by the KJMA model that incorporated two crystallization events. The fitted model parameters including incubation times and Avrami exponents were reported. The Avrami exponent of the primary crystallization event increased from 4.4 at 470 °C to 6.4 at 500 °C for the primary crystallization, which is understood as resulting from non-steady state homogeneous nucleation and 3-D interface-controlled growth. The Avrami exponent of the second crystallization event stayed relatively stable at around 2.6 to 2.8 across the seven temperatures, which is attributed to primary-crystal-induced heterogeneous nucleation and an effective sub-3-D growth mode. Cumulative transformation curves and corresponding TTT diagrams were obtained from the isothermal DSC data.
- XRD analysis of partially and fully crystallized specimens, both annealed at 475 °C in the calorimeter, identified the orthorhombic $Cu_{10}(Zr,Hf)_7$ to be the primary crystal phase and the tetragonal $Cu(Zr,Hf)_2$ to be the new phase produced in the second crystallization event. The phase identities were further confirmed by TEM using selected area electron diffraction.
- Analysis of the TEM image of the partially crystallized specimen revealed a high number density on the order of 10^{21} m^{-3}, a high nucleation rate of $\approx 10^{18}$ m^{-3} s^{-1}, and an extremely low growth rate of ≈0.38 nm/s of the primary crystals. These data suggest that between the nucleation and growth rates, the latter makes a greater contribution to the high glass-forming ability of this BMG. The high nucleation and low crystal growth rates imply that this BMG is particularly suitable to serve, through controlled devitrification, as a precursor to glass–nanocrystal composite or bulk nanocrystalline structures.

Author Contributions: Conceptualization, D.X.; methodology, D.X. and M.K.S.; validation, formal analysis, and investigation, J.S.S., T.D.K., T.T., L.C., M.K.S. and D.X.; resources, D.X. and M.K.S.; writing—original draft preparation, D.X.; funding acquisition, D.X. and M.K.S. All authors have read and agreed to the published version of the manuscript.

Funding: This research was partially supported by the U.S. National Science Foundation under grant Nos. DMR 2221854 and DMR 1945520.

Data Availability Statement: The data that support the findings of this study are available from the corresponding author upon reasonable request.

Acknowledgments: TEM was performed at the Oregon State University Electron Microscope Facility, which is supported by NSF MRI, grant no. 1040588; the Murdock Charitable Trust; and the Oregon Nanoscience and Micro-Technologies Institute.

Conflicts of Interest: The authors declare no conflict of interest.

References

1. Johnson, W.L. Bulk glass-forming metallic alloys: Science and technology. *MRS Bull.* **1999**, *24*, 42–56. [CrossRef]
2. Schroers, J. BULK Metallic Glasses. *Phys. Today* **2013**, *66*, 32–37. [CrossRef]
3. Loffler, J.F. Bulk metallic glasses. *Intermetallics* **2003**, *11*, 529–540. [CrossRef]
4. Greer, A.L. Metallic glasses. *Science* **1995**, *267*, 1947–1953. [CrossRef]
5. Inoue, A. Stabilization of metallic supercooled liquid and bulk amorphous alloys. *Acta Mater.* **2000**, *48*, 279–306. [CrossRef]
6. Schroers, J. The superplastic forming of bulk metallic glasses. *JOM* **2005**, *57*, 35–39. [CrossRef]
7. Schroers, J. Processing of Bulk Metallic Glass. *Adv. Mater.* **2010**, *22*, 1566–1597. [CrossRef]
8. Johnson, W.L.; Na, J.H.; Demetriou, M.D. Quantifying the origin of metallic glass formation. *Nat. Commun.* **2016**, *7*, 10313. [CrossRef]
9. Choi-Yim, H.; Xu, D.H.; Johnson, W.L. Ni-based bulk metallic glass formation in the Ni-Nb-Sn and Ni-Nb-Sn-X (X = B,Fe,Cu) alloy systems. *Appl. Phys. Lett.* **2003**, *82*, 1030–1032. [CrossRef]
10. Kim, W.; Oh, H.S.; Park, E.S. Manipulation of thermal and mechanical stability by addition of multiple equiatomic rare-earth elements in Al-TM-RE metallic glasses. *Intermetallics* **2017**, *91*, 8–15. [CrossRef]
11. Xu, D.H.; Lohwongwatana, B.; Duan, G.; Johnson, W.L.; Garland, C. Bulk metallic glass formation in binary Cu-rich alloy series—$Cu_{100-x}Zr_x$ (x = 34, 36 38.2, 40 at.%) and mechanical properties of bulk $Cu_{64}Zr_{36}$ glass. *Acta Mater.* **2004**, *52*, 2621–2624. [CrossRef]
12. Xu, D.H.; Duan, G.; Johnson, W.L.; Garland, C. Formation and properties of new Ni-based amorphous alloys with critical casting thickness up to 5 mm. *Acta Mater.* **2004**, *52*, 3493–3497. [CrossRef]
13. Xu, D.H.; Duan, G.; Johnson, W.L. Unusual glass-forming ability of bulk amorphous alloys based on ordinary metal copper. *Phys. Rev. Lett.* **2004**, *92*, 245504. [CrossRef] [PubMed]
14. Saini, J.S.; Palian, C.; Lei, F.Q.; Dyall, A.; AuYeung, N.; McQuade, R.; Gupta, S.K.; Cann, D.P.; Xu, D.H. Rare-earth and precious-metal free Cu-based metallic glasses with superior glass-forming ability and processability. *Appl. Phys. Lett.* **2020**, *116*, 011901. [CrossRef]
15. Saini, J.S.; Miska, J.P.; Lei, F.Q.; AuYeung, N.; Xu, D.H. Hafnium based metallic glasses with high density and high glass-forming ability. *J. Alloys Compd.* **2021**, *882*, 160896. [CrossRef]
16. Ponnambalam, V.; Poon, S.J.; Shiflet, G.J. Fe-based bulk metallic glasses with diameter thickness larger than one centimeter. *J. Mater. Res.* **2004**, *19*, 1320–1323. [CrossRef]
17. Zhang, M.; Song, Y.; Lin, H.; Li, Z.; Li, W. A Brief Introduction on the Development of Ti-Based Metallic Glasses. *Front. Mater.* **2022**, *8*, 814629. [CrossRef]
18. Sun, B.B.; Wang, Y.B.; Wen, J.; Yang, H.; Sui, M.L.; Wang, J.Q.; Ma, E. Artifacts induced in metallic glasses during TEM sample preparation. *Scr. Mater.* **2005**, *53*, 805–809. [CrossRef]
19. Blaine, R.L.; Kissinger, H.E. Homer Kissinger and the Kissinger equation. *Thermochim. Acta* **2012**, *540*, 1–6. [CrossRef]
20. Liu, L.; Wu, Z.F.; Zhang, J. Crystallization kinetics of $Zr_{55}Cu_{30}Al_{10}Ni_5$ bulk amorphous alloy. *J. Alloys Compd.* **2002**, *339*, 90–95. [CrossRef]
21. Mitrovic, N.; Roth, S.; Eckert, J. Kinetics of the glass-transition and crystallization process of $Fe_{72-x}Nb_xA_{l5}Ga_2P_{11}C_6B_4$ (x = 0.2) metallic glasses. *Appl. Phys. Lett.* **2001**, *78*, 2145–2147. [CrossRef]
22. Meng, C.F.; Chen, S.Y.; Qiao, M.Y.; Shao, Z.J. Determination of activation-energy for crystallization in metallic-glass by small-angle X-ray-scattering. *J. Non-Cryst. Solids* **1992**, *144*, 308–311. [CrossRef]
23. Cai, A.H.; Ding, D.W.; An, W.K.; Zhou, G.J.; Luo, Y.; Li, J.H.; Peng, Y.Y. Effect of Ni substitution on glass forming ability, mechanical, electrical and thermal properties of Cu-Zr-Ti glass forming alloys. *Mater. Chem. Phys.* **2015**, *151*, 243–251. [CrossRef]
24. Park, S.O.; Lee, J.C.; Kim, Y.C.; Fleury, E.; Sung, D.S.; Kim, D.H. Crystallization kinetics of the $CU_{43}Zr_{43}Al_7Ag_7$ amorphous alloy. *Mater. Sci. Eng. A-Struct. Mater. Prop. Microstruct. Process.* **2007**, *449*, 561–564. [CrossRef]
25. Duan, G.; Xu, D.H.; Zhang, Q.; Zhang, G.Y.; Cagin, T.; Johnson, W.L.; Goddard, W.A. Molecular dynamics study of the binary $Cu_{46}Zr_{54}$ metallic glass motivated by experiments: Glass formation and atomic-level structure. *Phys. Rev. B* **2005**, *71*, 224208. [CrossRef]
26. Kelton, K.F.; Gangopadhyay, A.K.; Kim, T.H.; Lee, G.W. A case for local icosahedral order in undercooled metallic liquids and the influence on the nucleation barrier. *J. Non-Cryst. Solids* **2006**, *352*, 5318–5324. [CrossRef]
27. Xu, D.H.; Chen, F.Z. Continuously variable atomic structure in monatomic metallic glasses through active icosahedral dynamics below glass transition temperature. *J. Appl. Phys.* **2018**, *124*, 125101. [CrossRef]
28. Xu, D.H.; Wang, Z.M.; Chang, T.Y.; Chen, F.Z. Inverted core-shell potential energy landscape of icosahedral clusters in deeply undercooled metallic liquids and glasses and its effect on the glass forming ability of bcc and fcc metals. *J. Phys.-Condens. Matter* **2020**, *32*, 405402. [CrossRef]
29. Chang, T.Y.; Wang, Z.M.; Xu, D.H. Formation energetics/dynamics of icosahedral clusters in supercooled metallic liquids in the dynamic equilibrium regime: Gibbs free energy, entropy, enthalpy, and connection to coordination shells. *J. Mater. Res.* **2023**, *38*, 179–186. [CrossRef]
30. Chang, T.Y.; Wang, Z.M.; Xu, D.H. Icosahedral clusters in $Cu_{100-x}Zr_x$ (x = 32, 34, 36, 38.2, 40 at.%) metallic glasses near the peak of glass-forming ability (x = 36): A balance between population and encaging strength. *J. Phys. Chem. Solids* **2021**, *154*, 110076. [CrossRef]

31. Doebelin, N.; Kleeberg, R. Profex: A graphical user interface for the Rietveld refinement program BGMN. *J. Appl. Crystallogr.* **2015**, *48*, 1573–1580. [CrossRef] [PubMed]
32. Jain, A.; Ong, S.P.; Hautier, G.; Chen, W.; Richards, W.D.; Dacek, S.; Cholia, S.; Gunter, D.; Skinner, D.; Ceder, G.; et al. Commentary: The Materials Project: A materials genome approach to accelerating materials innovation. *Appl. Mater.* **2013**, *1*, 011002. [CrossRef]
33. Gates-Rector, S.; Blanton, T. The Powder Diffraction File: A quality materials characterization database. *Powder Diffr.* **2019**, *34*, 352–360. [CrossRef]
34. Schneider, C.A.; Rasband, W.S.; Eliceiri, K.W. NIH Image to ImageJ: 25 years of image analysis. *Nat. Methods* **2012**, *9*, 671–675. [CrossRef] [PubMed]
35. Xu, D.H.; Johnson, W.L. Crystallization kinetics and glass-forming ability of bulk metallic glasses Pd40Cu30Ni10P20 and $Zr_{41.2}Ti1_{3.8}Cu_{12.5}Ni_{10}Be_{22.5}$ from classical theory. *Phys. Rev. B* **2006**, *74*, 024207. [CrossRef]